CERN-ACC-NOTE-2019-0032
August 2, 2019
xavier.buffat@cern.ch

Mode coupling instability of colliding beams in the HL-LHC

L. Barraud and X. Buffat
CERN, Geneva, Switzerland

Abstract

The coupling between the coherent beam-beam modes and the head-tail modes can result in strong instabilities under the effect of electromagnetic wake fields. This mode coupling phenomenon was modelled and observed in the Large Hadron Collider (LHC) for the dipole mode. In the High Luminosity upgrade (HL-LHC), the low β function at the interaction point may generate coupling instabilities of higher-order head-tail modes which would not be stabilised by the transverse feedback. This paper describes the development of an efficient 6D model of the coherent beam-beam interactions in order to assess the beam stability in configurations relevant for the HL-LHC. After having described the limit of the simulation method, we show that the mechanism of Landau damping by the synchrotron sidebands of the incoherent spectrum is sufficient to stabilise the beam in the operational scenario of HL-LHC, including a backup scenario without crab-cavity featuring a large Piwinski angle.

Keywords: LHC, HL-LHC, HiLumi LHC, coherent beam-beam effect, beam instabilities, Landau damping, crossing angle, hourglass effect

Contents

1 Introduction

The beam-beam interaction is a source of coupling between the colliding beams. Once coupled, a system of two identical beams feature two modes oscillation [1] corresponding to in phase motion of the two beams, the so-called σ-mode, with a frequency at the unperturbed tune, or out-of-phase motion, corresponding to the π-mode, with a frequency shifted with respect to the unperturbed tune proportionally to the strength of the beam-beam force. These two modes could couple with the natural higher order transverse modes of oscillation of each beam, the so called head-tail modes and be driven unstable by the electromagnetic wake fields resulting from the interaction of the charged particles with their surrounding. This so-called mode coupling instability of colliding beams was studied for the Large Hardron Collider (LHC) [2], showing a strong instability resulting from the coupling of the azimuthal head-tail mode ± 1 with the beam-beam modes σ and π. In absence of variations of the beam-beam force along the bunch length, due to a crossing angle between the beams or due to the so-called hourglass effect, the beam-beam force is mainly dependent on the first-order moment, or dipolar moment, of the transverse mode of oscillation. The LHC is equipped with a transverse feedback acting on the dipolar motion and, consequently, was found to be efficient against the mode coupling instability of colliding beams of low order mode. However, the variation of the beam-beam force over the bunch length, generating the so-called synchrobetatron coupling, allows for coupling of higher order modes for which the current transverse feedback is inefficient. Such an effect was shown in [3] using a linearised model implemented in the code *BimBim* [4]. Due to the linearisation, the tune spread induced by the beam-beam interactions is neglected, this model is therefore not suited for the estimation of Landau damping. On the other hand, synchrobetatron coupling was identified as a mechanism enabling Landau damping of coherent beam-beam modes by the synchrotron sidebands of the incoherent spectrum [5, 6] with the potential of damping the resulting high order mode coupling instability. The effect is however not quantified, in particular in term of acceptable impedance. The goal of this study is to develop a numerical model of the mode coupling instability of colliding beams including the non-linearities of the beam-beam force, i.e. Landau damping, synchrobetatron coupling and the effect of the wake fields in order to eventually use it to estimate the beam stability in the HL-LHC configurations.

While such an implementation already exists in the code *BeamBeam3D* [7], the large computational requirements led us to a more efficient simplified implementation, yet maintaining the accuracy of the predictions for the HL-LHC configuration. Thus, we start by describing two models : a full implementation and a computationally more efficient model, based on a frozen beam distribution during a bunch crossing resulting in a limited domain of validity. The single particle aspect of this implementation of the 6D beam-beam interaction in the macroparticle code *COMBI* [4, 8–10] is then benchmarked against the original weak-strong code [11]. The coherent aspect is also benchmarked against theoretical predictions via the Yokoya Factor [12]. The limits of the frozen model are then explored, before investing numerically the link between the decoherence and the Landau Damping shown in [5]. Finally, the results of parametric studies of the mode coupling instability of colliding beams in the HL-LHC operational scenario are exposed.

2 Numerical Model of the 6D beam-beam strong-strong soft-Gaussian kick

To quantify the Landau Damping effect, we need a more accurate model than the linearised modal approach. In particular, a model of the single particle motion in the presence of the strong non-linearity of the beam-beam force, along with a model of the coherent force is required. In this section we present the way to model the evolution of two bunches across each other over multiple turns using the macro-particle approach, based on the existing code *COMBI*. In order to take into account the effect of the crossing angle at the Interaction Point (IP), as well as the effect of the variation of the beam size over the length of the interaction, due to the low β^* in comparison to the bunch length σ_s, we compute the kick on every single particle based on an adaptation of the weak-strong algorithm developed in [11] which takes into account the statistical moments of the other beam's particle distribution evaluated numerically rather than the assumed values for the other beam.

The principle of the algorithm is as follows. For each colliding bunch, we perform the Lorentz boost of the coordinate of each macro-particle from the laboratory frame to a referential moving transversely to the propagation axis of the two beams, such that the crossing angle between the beams appears cancelled in this frame, as a result the bunch distributions are tilted in this new frame, as illustrated in Fig. 1. Second, we sort the particles of each bunch in N_s equidistant longitudinal slices and compute their first and second statistical moments based on the coordinates of the macro-particles contained in each slice in the boosted frame. Then, we compute the variation of the momentum of each particle based on the derivation of the electromagnetic fields for a Gaussian distribution of charges due to each colliding bunch slice. Finally, we perform the inverse boost to restore the coordinate of each beam in its own frame. As opposed to the weak-strong model, the moments of the slices have, in principle, to be recomputed after every slice-slice interaction, since the trajectory of the particles is modified by the electromagnetic interaction. Such a so-called full implementation is computationally expensive, as the statistical moments needs to be computed N_s^2 times. In some cases however, the variation of the particles' trajectories over a single interaction between two bunches, and the resulting modification of the electromagnetic force, is negligible. In such configurations, the computational needs can be reduced by computing the slice moments only once at the start of the interaction, thus neglecting the effect of the beam-beam interaction. This method is somewhat intermediate between a weak-strong model, where the reaction of the other beam is entirely neglected and a full strong-strong model, since it neglects the reaction of the other beam only through a single interaction, but does model properly the variations turn after turn. This frozen model can therefore be used to describe the coherent modes only when the beam-beam interaction is sufficiently weak. The next section describes the mathematical details of these implementations, including the derivation of a criterion for the validity of the frozen model.

2.1 6D beam-beam soft Gaussian kick

2.1.1 Lorentz Boost

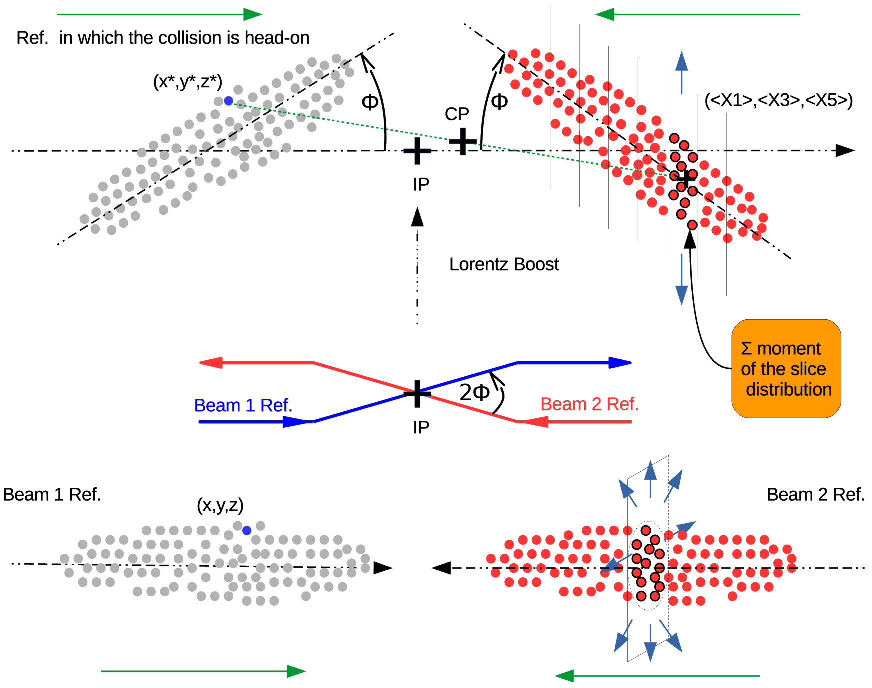

Figure 1: Schematic view of the distributions of macro-particles of the two beams in their own reference frame, i.e. with respect to their own closed orbit at the IP, as modelled in *COMBI* (lower plot). The closed orbit of the two beams, including the crossing angle is shown in the middle plot. Finally the upper sketch shows the distribution of the macro-particle distribution in a boosted frame that cancels the crossing angle between the beams. The interaction between a macro-particle (blue dot) and a slice of the opposing beam (black circled red dots) is illustrated with a green dashed line. The fields are computed at the Collision Point (CP) defined by the location where the particle and the slice are at the same longitudinal position, based on the statistical moments of the distribution of the macro-particle in the slice.

Figure 1 illustrates two bunches colliding with a crossing angle ϕ at the IP in their own reference frame and around their own closed orbit (i.e. corresponding to half the total crossing angle between the beams), as well as the boost in the common frame where the collision is head-on. Considering the quadrivector conservation in the ultra-relativistic approximation, the boost can be written [13, 14]:

$$\begin{cases} x^* = z\cos\alpha\tan\phi + x[1 + h_x^*\cos\alpha\sin\phi] + yh_x^*\sin\alpha\sin\phi \\ y^* = z\sin\alpha\tan\phi + y[1 + h_y^*\sin\alpha\sin\phi] + xh_y^*\cos\alpha\sin\phi \\ z^* = \frac{z}{cos\phi} + h_z^*[x\ \cos\alpha\sin\phi + y\ \sin\alpha\sin\phi] \end{cases} \tag{2.1}$$

$$\begin{cases} p_x^* = \frac{p_x}{cos\phi} - h\cos\alpha\frac{tan\phi}{cos\phi} \\ p_y^* = \frac{p_y}{cos\phi} - h\sin\alpha\frac{tan\phi}{cos\phi} \\ \frac{dp}{p}^* = \frac{dp}{p} - p_x\cos\alpha\tan\phi - p_y\sin\alpha\tan\phi - h\tan^2\phi \end{cases} , \tag{2.2}$$

where α is the angle between the crossing angle plane and the s,x plane, $(x, y, z, p_x, p_y, dp/p)$ are the coordinates of the beam in its own frame, the corresponding Hamiltonian is given by:

$$h = 1 + \frac{dp}{p} - \sqrt{\left(1 + \frac{dp}{p}\right)^2 - p_x^2 - p_y^2}, \tag{2.3}$$

and in the boosted frame:

$$h_x^* = \frac{p_x^*}{\sqrt{\left(1 + \frac{dp^*}{p^*}\right)^2 - p_x^{*2} - p_y^{*2}}} \tag{2.4}$$

$$h_y^* = \frac{p_y^*}{\sqrt{\left(1 + \frac{dp^*}{p^*}\right)^2 - p_x^{*2} - p_y^{*2}}} \tag{2.5}$$

$$h_z^* = 1 - \frac{\frac{dp^*}{p^*} + 1}{\sqrt{\left(1 + \frac{dp^*}{p^*}\right)^2 - p_x^{*2} - p_y^{*2}}}. \tag{2.6}$$

(2.7)

2.1.2 *Computation of the statistical moment*

As illustrated in Fig. 1, the particles of the bunch are sorted in N_s longitudinal slices. The first and second statistical moments of the distribution of slice k are computed based on the 6D coordinates of the macro-particles inside each slice, $X^k = (x, p_x, y, p_y, z, \frac{dp}{p})$, noted $\left\langle X_i^k \right\rangle$ and Σ_{ij}^k respectively, with $i, j = 1, ..., 6$. The IP is defined as the longitudinal location where the bunch centres cross each other. In the ultra relativistic approximation, the electromagnetic fields are purely transverse, as illustrated with blue arrows on Fig. 1. Consequently, the beam-beam forces between a given macro-particle and a slice has to be computed at the corresponding Collision Point (CP), where the two are located at the same longitudinal position (Fig. 1). The longitudinal distance between the CP and the IP for a given macro-particle and slice k is given by:

$$S_z = \frac{z^* - \left\langle X_5^k \right\rangle}{2}. \tag{2.8}$$

At the CP, the distance between the slice centroid and a given macro-particle is:

$$S_{\{x,y\}} = \left(\{x,y\}^* + p^*_{\{x,y\}} S_z\right) - \left(\left\langle X^k_{\{1,3\}} \right\rangle - \left\langle X^k_{\{2,4\}} \right\rangle S_z\right). \tag{2.9}$$

The variation of the transverse position due to the crossing angle is now embedded in the momentum of the particles in the boosted frame. The variation of the β function with the longitudinal position results in a modification of the beam sizes $\sigma^k_{\{x,y\}}(S_z)$, which is taken into account as follows [13]:

$$\begin{aligned}
\sigma_x^k(S_z) &= \Sigma_{11}^k + 2\Sigma_{12}^k S_z + \Sigma_{22}^k {S_z}^2 && (2.10)\\
\sigma_y^k(S_z) &= \Sigma_{33}^k + 2\Sigma_{34}^k S_z + \Sigma_{44}^k {S_z}^2. && (2.11)
\end{aligned}$$

2.1.3 *Computation of the slice-macro-particle interaction*

The variation of the transverse momentum of a particle experiencing the electromagnetic forces generated by a Gaussian beam integrated over the collision was derived in [1]. For completeness, we write here the algorithm as implemented in *COMBI* without derivation. Let us define the strength of the interaction based on the number of particles in the slice N^k, the classical proton radius r_0 and the relativistic γ factor:

$$f_0^k = -\frac{N^k r_0}{\gamma}. \tag{2.12}$$

We can then write:

$$F^k_{\{x,y\}}(S_x, S_y, S_z) = f_0^k \sqrt{\frac{2\pi}{\eta^k}} \{\mathrm{Im},\mathrm{Re}\} \left[\mathrm{w}\left(\frac{S_x + iS_y}{\sqrt{2\eta^k}}\right) - \exp\left(-\frac{{S_x}^2}{2\sigma_x^{k2}} - \frac{{S_y}^2}{2\sigma_y^{k2}}\right) \mathrm{w}\left(\frac{\frac{\sigma_y^k(S_z)}{\sigma_x^k(S_z)} S_x + i\frac{\sigma_x^k(S_z)}{\sigma_y^k(S_z)} S_y}{\sqrt{2\eta^k}}\right)\right], \tag{2.13}$$

where w is the error function and:

$$\eta^k = \sigma_x^k(S_z)^2 - \sigma_y^k(S_z)^2. \tag{2.14}$$

Implicitly, $\sigma_x^k > \sigma_y^k$ is assumed here. The longitudinal component of the integrated force can be expressed in function of the transverse components:

$$F_z^k(S_x, S_y, S_z) = S_z\left(\Sigma_{22}^k G_x^k + \Sigma_{44}^k G_y^y\right) + \frac{1}{2}\left[F_x^k\left(p_x^* - \frac{F_x^k}{2}\right) + F_y^k\left(p_y^* - \frac{F_y^k}{2}\right)\right], \tag{2.15}$$

where:

$$G^k_{\{x,y\}}(S_x, S_y, S_z) = \{-,+\}\sqrt{\frac{2}{\chi(S_z)}}\left[S_x F_x^k + S_y F_y^k + f_0^k\left[\frac{\sigma^k_{\{x,y\}}(S_z)}{\sigma^k_{\{y,x\}}(S_z)} e^{-\left(\frac{x^2}{2\sigma_x^k(S_z)} + \frac{y^2}{2\sigma_y^k(S_z)}\right)} - 1\right]\right], \tag{2.16}$$

with:

$$\chi(S_z) = \sigma_x^k(S_z) - \sigma_y^k(S_z). \tag{2.17}$$

Finally we obtain the new coordinates of each macro-particle of the bunch due the electromagnetic force of all the slices [13]:

$$\begin{cases}
x^*_{new} &= x^* + S_z F_x^k(S_x, S_y, S_z)\\
p^*_{x,\mathrm{new}} &= p_x^* - F_x^k(S_x, S_y, S_z)\\
y^*_{new} &= y^* + S_z F_y^k(S_x, S_y, S_z)\\
p^*_{y,\mathrm{new}} &= p_y^* - F_y^k(S_x, S_y, S_z)\\
z^*_{new} &= z^*\\
\frac{dp}{p}^*_{\mathrm{new}} &= \frac{dp}{p}^* - F_z^k(S_x, S_y, S_z).
\end{cases}$$

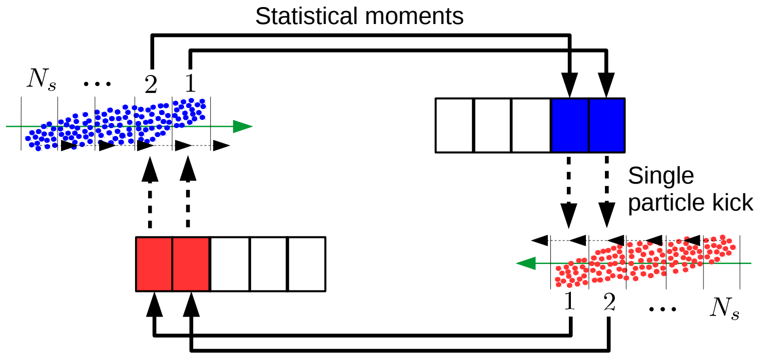

Figure 2: Illustration of the iterative method for the computation of the coherent 6D kick. At each step, the statistical moments of the colliding slices (here the first and the second) of the two beams is computed and communicated via MPI (solid lines) and then the kick applied to the single particles in the other beam (dashed lines). The particles of each slices are transported to the location of the next interaction, with the next slice of the other beam (dotted lines).

2.1.4 Iteration over the slices

In order to obtain a complete description of the interaction, a computation of the effect of each slice on every particle of the other beam needs to be computed iteratively respecting causality and including a re-evaluation of the statistical moments at every step due to the change in momentum generated by the interaction itself. This can be done with $n = 1,..,2N_s-1$ steps, at which the statistical moments of the slices with $k \in [\max(1,n-N_s+1),\min(n,N_s)]$ are computed and the interaction of these slices with the particles in the corresponding slice $n-k+1$ of the other beam is evaluated as described previously. This iterative method is illustrated in Fig. 2. In order to fit the parallel computing paradigm of *COMBI*, the statistical moments of each slice are computed by the *MPI* process holding the memory with coordinates of the macro-particles in the beams, only the information of the statistical moments of the slices is sent to the *MPI* process holding the coordinates of the colliding bunch of the other beam. This process then computes the effect of the slices on the corresponding macro-particles, using a second level of parallelisation based on *OpenMP*.

This method requires multiple evaluations of the statistical moments of each slice which becomes particularly heavy when a large number of macro-particles are required to model the interaction accurately. The computational requirement can be relaxed for configurations where the deflections due to the beam-beam interactions with the slices are weak, such that the variation of the statistical moments over one interaction is negligible and consequently do not need to be re-evaluated at every step. This condition is met if the effect of the maximum transverse deflection over the interaction length, which we pessimistically consider equal to the bunch length, remains small when compared to the beam size. In this case, we can write:

$$\frac{\max\limits_{x',y',s',k} F^k_{\{x,y\}}(x',y',s')\sigma_s}{\sigma_x} << 1. \tag{2.18}$$

Remaining pessimistic, we derive the maximum of the kick neglecting the longitudinal variations of the force and the crossing angle and we assume round Gaussian beams. The integrated beam-beam force in the horizontal plane is given by:

$$F_x(x,y) = \frac{2Nr_0}{\gamma}\frac{x}{r^2}\left[1-e^{(-\frac{r^2}{2\sigma^2})}\right], \tag{2.19}$$

with $r = \sqrt{x^2+y^2}$. The maximum of the force is given by:

$$\left(\frac{2x^2}{2\sigma_x^2}+1\right)e^{-\frac{x^2}{2\sigma_x^2}} = 1, y = 0. \tag{2.20}$$

The solution $x_{\max}$ can be expressed using the lower branch of the Lambert function W_{-1} [15]:

$$\frac{x^2_{\max}}{2\sigma^2} = -W_{-1}\left(-\frac{1}{2\sqrt{2\sqrt{e}}}\right)-\frac{1}{2} \approx 1.2563. \tag{2.21}$$

Finally we obtain for the maximum:

$$\max_{x,y} F_x(x,y) = \frac{2Nr_0}{\gamma x_{\max}}\left[1-e^{-\frac{x^2_{\max}}{2\sigma^2}}\right] \approx 0.9025\frac{Nr_0}{\gamma\sigma}. \tag{2.22}$$

The criterion 2.18 roughly becomes:

$$\chi_{\text{frozen}} \equiv \frac{Nr_0}{\varepsilon}\frac{\sigma_s}{\beta^*} << 1, \tag{2.23}$$

where we recognise a dependence on the beam-beam parameter $(Nr_0/4\pi\varepsilon)$ and on the hourglass parameter σ_s/β^*. The frozen model is therefore appropriate for reasonably low beam-beam parameter and weak hourglass effect.

In the HL-LHC operational scenario [16], the strongest head-on beam-beam interaction is obtained at the start of collision in the ultimate scenario, where we have $\chi_{\text{frozen}} \approx 0.03$, justifying the relevance of the frozen model in the various HL-LHC configurations. Indeed, the most critical configuration is at the edge of numerical artefacts linked to this approximation, as will be discussed in Sec. 2.3.

2.1.5 Reverse Lorentz Boost

After the computation of the new coordinates in the boosted frame, we perform the corresponding anti Lorentz Boost to obtain the coordinates of the macro-particles of each beam in their own reference frame. Again following [14], we have:

$$\begin{aligned}
x_{new} &= (x^*_{new}[\frac{1}{\cos\phi} + sin\alpha\tan\phi(h^*_{y,\text{new}} - h^*_{z,\text{new}}\sin\alpha\sin\phi)] \\
&+ y^*_{new}\sin\alpha\tan\phi[h^*_{z,\text{new}}\cos\alpha\sin\phi - h^*_{x,\text{new}}] \qquad (2.24)\\
&- z^*_{new}\tan\phi[\cos\alpha - h^*_{x,\text{new}}sin^2\alpha\sin\phi + h^*_{y,\text{new}}\cos\alpha\sin\alpha\sin\phi])/\det(L) \\
y_{new} &= (x^*_{new}\cos\alpha\tan\phi[-h^*_{y,\text{new}} + h^*_{z,\text{new}}\sin\alpha\sin\phi] \\
&+ y^*_{new}[\frac{1}{\cos\phi} + \cos\alpha\tan\phi(h^*_{x,\text{new}} - h^*_{z,\text{new}}\cos\alpha\sin\phi)] \qquad (2.25)\\
&- z^*_{new}\tan\phi[\sin\alpha - h^*_{y,\text{new}}cos^2\alpha\sin\phi + h^*_{x,\text{new}}\cos\alpha\sin\alpha\sin\phi])/\det(L) \\
z_{new} &= (-x^*_{new}h^*_{z,\text{new}}\cos\alpha\sin\phi \qquad (2.26)\\
&- y^*_{new}h^*_{z,\text{new}}\sin\alpha\sin\phi \\
&+ z^*_{new}[1 + h^*_{x,\text{new}}\cos\alpha\sin\phi + h^*_{y,\text{new}}\sin\alpha\sin\phi])/\det(L),
\end{aligned}$$

where the determinant of the matrix L representing the transformation of Eq. 2.1 was introduced:

$$\det(L) = \frac{1}{cos\phi} + \left(h^*_{x,\text{new}}cos\alpha + h^*_{y,\text{new}}sin\alpha - h^*_{z,\text{new}}sin\phi\right). \qquad (2.27)$$

By recomputing the Hamiltonian h and inverting the system 2.2, we find the corresponding momentum :

$$\begin{cases}
p_{x,\text{new}} = p^*_{x,\text{new}\cos\phi} + h\cos\alpha\tan\phi \\
p_{y,\text{new}} = p^*_{y,\text{new}} + h\sin\alpha\tan\phi \\
\frac{dp}{p}_{\text{new}} = \frac{dp}{p}^*_{\text{new}} - p_x\cos\alpha\tan\phi - p_y\sin\alpha\tan\phi - h\tan^2\phi.
\end{cases} \qquad (2.28)$$

2.2 Benchmark

This section summarises convergence studies of the algorithm implemented against the weak-strong code *BBC* [11] as well as a test of the coherent component of the algorithm by recovering the Yokoya factor [12] for the frequency of the beam-beam π-mode. The theoretical result is also extended with these simulations to configurations with a crossing angle.

2.2.1 Convergence against the weak-strong model

Table 1: Parameters used for the benchmark of the code and for the simulation of the HL-LHC. We shall note that the latter differ slightly from the present baseline [16]. The partial compensation of the crossing angle by crab cavities is modelled with an effective crossing angle. The wake field model is detailed in [17, 18]. 500 longitudinal slices were used for the numerical modelling of the effect of the wake fields.

	Benchmark	**HL-LHC**
Energy $[TeV]$	7.0	
Intensity N_b $[10^{11}\ p/b]$	1.1	2.2
β^* $[m]$	0.6	0.15
Transverse Emittance ε_n $[\mu m]$	2	2.5
Longitudinal size σ_s $[ns]$	0.25	0.3
Rel. energy spread σ_p $[10^{-4}]$	1.129	1.2
Betatron tunes (H/V)	0.31 / 0.32	
Synchrotron tune	0.0012	
Full effective crossing angle $[\mu\text{rad}]$	140	

This implementation of the 6D electromagnetic model was benchmarked with the reference code *BBC* [11]. This reference code computes the momentum variation of a single particle experiencing the electromagnetic forces of the other beam, taking into account the effect of the crossing angle and the hourglass effect, assuming a Gaussian distribution of the charges. Contrary to *COMBI*, the distribution of the other beam, i.e. the strong beam, is known and remains unchanged. The dynamics of the coherent instabilities requires a dynamical model of the distribution of each beam and therefore can only be modelled with *COMBI*. Consequently, the physics of the two codes is expected to be identical on the first turn of the simulation since the macro-particles are initialized with a Gaussian distribution in COMBI.

For the benchmark, we fixed the number of slices at 50 in the *BBC* input parameter. We compute for different numbers of macro-particle and numbers of slices the distribution after one interaction with *COMBI*. In input of the *BBC* software we used the random Gaussian distribution generated by *COMBI* before the first turn, such that the result of the two codes can be directly compared.

After the computation of the boost, kick due to the beam-beam interaction and inverse boost for one turn, we compare the two output distributions using the error definition:

$$\Delta_i^{COMBI} = \frac{\langle \left| \Delta p_i{}^{\mathrm{COMBI}} - \Delta p_i{}^{\mathrm{BBC}} \right| \rangle}{\langle \left| \Delta p_i{}^{\mathrm{BBC}} \right| \rangle}, \tag{2.29}$$

where Δp_i is the difference in momentum due to the electromagnetic interaction at the IP for one turn with $i = x, y, z$. The error is expressed relatively to the average value of the kick computed with the reference code *BBC*. In Eq. 2.29, $\langle \left| \Delta p_i{}^{\mathrm{BBC}} \right| \rangle$ represents the average of the absolute value of the difference in momentum computed with *BBC* code:

$$\langle \left| \Delta p_i{}^{\mathrm{BBC}} \right| \rangle = \frac{1}{N_m} \sum_{n=0}^{N_m} \left| \Delta p_i^{n\mathrm{BBC}} \right|, \tag{2.30}$$

where N_m is the number of macroparticle and Δp_i^n is the difference in momentum corresponding to the macroparticle n.

Fixing the number of slices in *COMBI* to 30, we obtained an error decreasing with $\approx N_m^{-0.5}$ (Fig. 3a). This convergence of the error is in agreement with the typical statistical error on the computation of the moments, which is required in *COMBI* but not in *BBC*. Fixing the number of macro-particles to 10^6, we observed a strong decrease of the error between 1 slice and 7 slices (Fig. 3b). For the low number of slices the field variations due to the crossing angle could not be captured, resulting in a strong inaccuracy. Once a sufficient number of slices is reached, the error decreases much slower, close to the expected statistical convergence. More generally, the convergence is shown as a function of the two numerical parameters in Fig. 4. We observe that the accuracy is mainly limited by the large number of macro-particles required, whereas approximatively 10 slices are sufficient to reach the convergence in this numerical parameter. With 10^6 macro-particles, the remaining error is $\approx 5 \cdot 10^{-3}$, which is considered acceptable for the simulations of fast collective effects, as the error does not increase linearly with time due to the mixing of the particles as they perform betatron oscillation in the presence of a strong non-linear force.

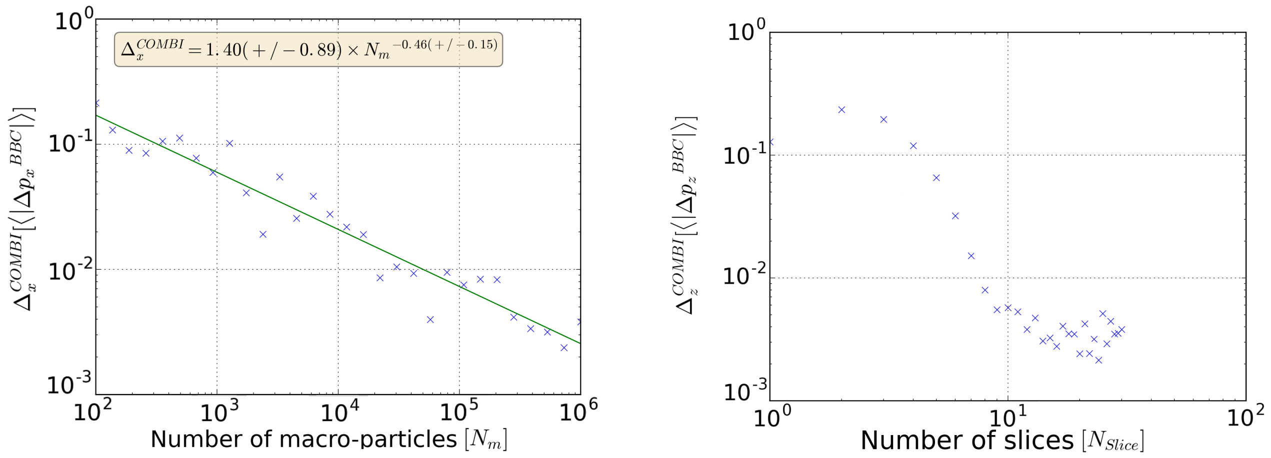

(a) Δ_x^{COMBI} in function of the number of macro-particles (N_m) for a number of slice (N_{Slice}) fixed at 30.

(b) Δ_z^{COMBI} in function of the number of slice (N_{Slice}) for a number of macro-particle (N_m) fixed at 10^6.

Figure 3: Relative difference in the 6D beam-beam kick in *COMBI* and *BBC* as a function of the number of macro-particles (left plot) and the number of slices (right plot), using the benchmark configuration described in Tab. 1. The horizontal and longitudinal kicks are shown, the same behaviour is observed in all degrees of freedom.

2.2.2 The Yokoya factor

When we consider two beams travelling through identical lattices and experiencing a single beam-beam interaction, the dipole coherent modes of oscillation are the σ-mode and π-mode visible in the oscillation spectrum of the beams shown in Fig. 5. The results of several simulations with different crossing angles are shown. For comparison the frequency obtained with the linearised model are shown with dots. Red dots represent dipole modes whereas the light yellow dots show higher order head-tail modes, which are therefore not visible in the beam spectrum. The dependence of the π-mode on the crossing angle is similar for both the modal approach and the macro-particles tracking simulations. The crossing angle is on the (x, s)-plane but the dependence of the angle is also visible in the perpendicular direction y as it also introduces a, yet weaker, variation of the force in the non-crossing plane.

The frequency difference of the π-mode between the two approaches is due to variation of the beam distribution caused by non-linearity of the beam-beam interaction which is only modelled by the macro-particle approach. The

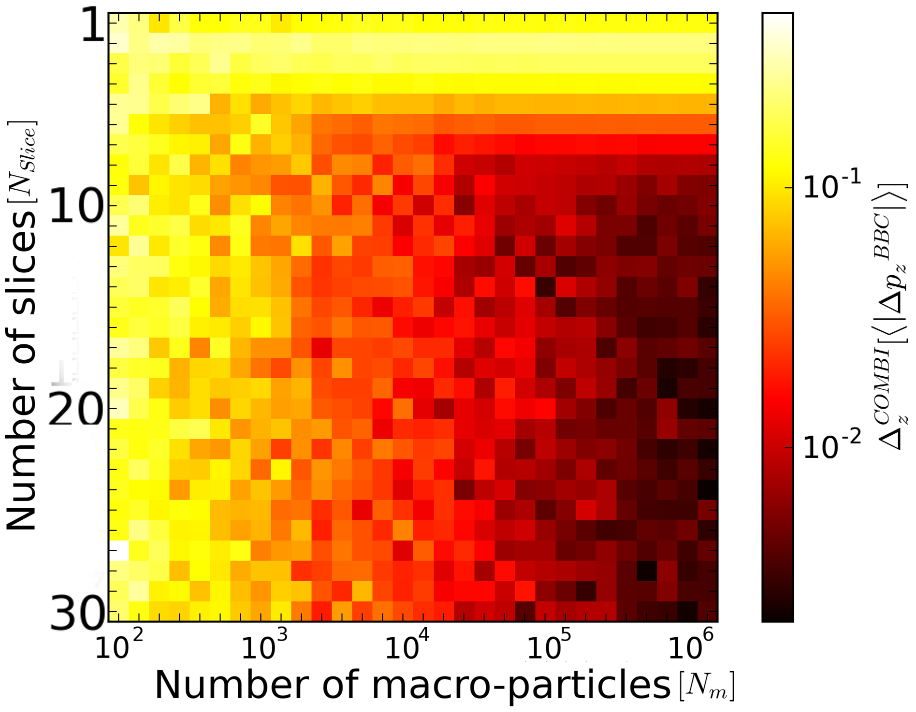

Figure 4: Convergence of Δ_z^{COMBI} as function of the two numerical parameters, namely the number of macro-particles and of slices. The configuration considered for this benchmark is a variation of the HL-LHC configuration described in Tab. 1 but with $\beta^* = 10\ m$ and a full crossing angle of 500μrad.

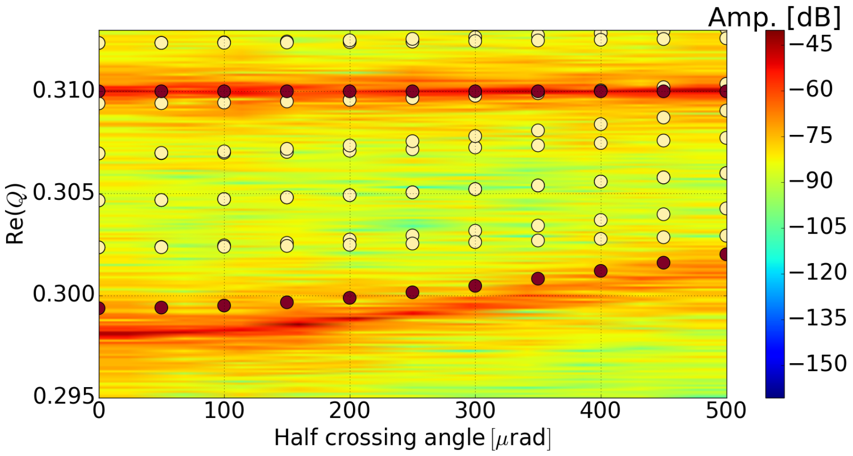

(a) x-component.

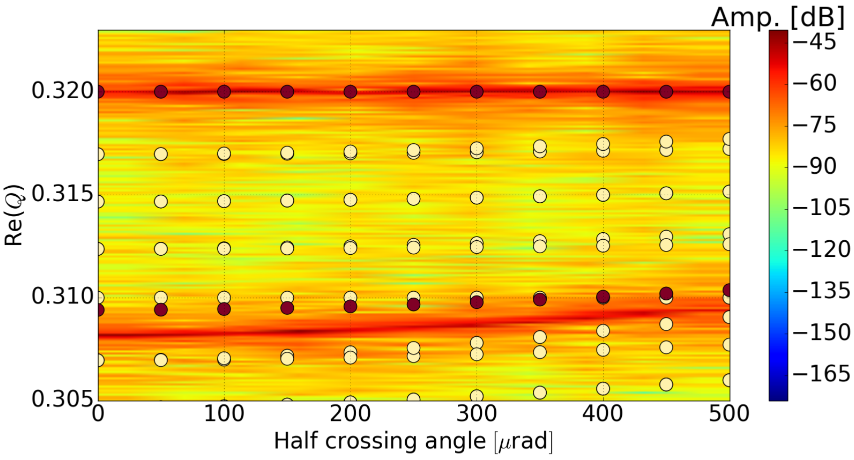

(b) y-component.

Figure 5: Comparisons of the real part of the frequency between the modal analysis with *BimBim* (The red and yellow dots represent mode with a large and small dipole moment respectively) and the macro-particle with 6D soft Gaussian beam-beam kick *COMBI* (spectogram) for a variation of the HL-LHC configuration described in Tab. 1 but with $\beta^* = 10\ m$ and a full crossing angle of 500μrad. This simulation includes the effect of the lattice, the beam-beam interaction and a beam-beam interaction at a single IP with the crossing angle in the (x, s)-plane. The macro-particle simulations are based on the tracking of 10^6 particles over 10^4 turns. The coherent 6D beam-beam interaction is modelled with 15 slices. The modal approach is based on a discretisation of the longitudinal phase space with 4 slices a single ring, i.e. corresponding to the so-called air-bag model for the longitudinal phase space.

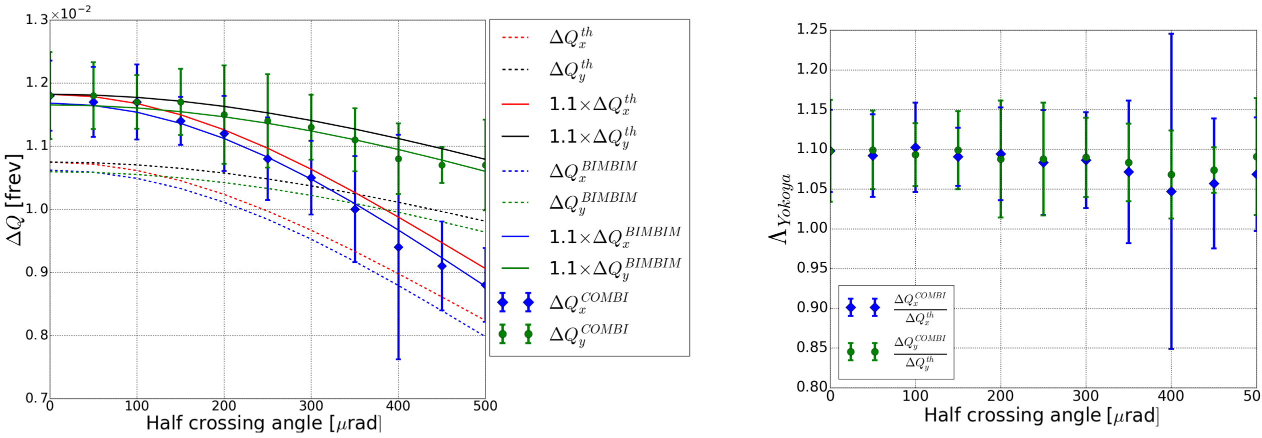

(a) The ΔQ between the σ-mode and π-mode. (b) The Yokoya factor.

Figure 6: Tune shift between the π-mode and σ-mode as a function of the crossing angle based on the spectrum shown in Fig. 5, the linearised model and a theoretical estimate, with the Yokoya factor deducted. The error bar is evaluated based on the width of the π-mode peak in the oscillation spectrum of beam in the macro-particle simulation shown in Fig. 7.

variation is described with a form factor called the Yokoya factor [12]. As the coherent 6D beam-beam kick is based on a soft-Gaussian approximation, it is expected to find $\Lambda_{\text{Yokoya}} \approx 1.1$.
The theoretical tune shift in the presence of a crossing angle, neglecting coherent effects, ΔQ^{th} can be obtained by computing the tune shift for a 4D beam-beam interaction and adjusting the beam size in the crossing angle plane using the so-called effective beam size. Given the Piwinski angle:

$$P_{x,y} = \frac{\sigma_s}{\sigma_{x,y}}\frac{\phi}{2}, \tag{2.31}$$

with $\sigma_{x,y}$ the r.m.s. transverse beam size in the plane of the crossing angle, we can write :

$$\Delta Q_x^{th} = \frac{N_b r_0 \beta_x^*}{2\pi\gamma\sigma_x^0\sqrt{1+{P_x}^2}\left(\sigma_x^0\sqrt{1+{P_x}^2}+\sigma_y\right)}. \tag{2.32}$$

Figure 6a shows a comparison of the tune shift between the σ and π modes obtained with the different approaches. The frequency tune shift obtained with the linearised modal approach is noted ΔQ^{BIMBIM}. While the results obtained with COMBI (points) are not compatible with the modal approach and the theoretical model without form factor (dashed lines), they are compatible with the same curve assuming $\Lambda_{\text{Yokoya}} \approx 1.1$. The Yokaya factor directly estimated from this comparison is shown in Fig. 6b. The results obtained not only are in agreement with the theory at zero crossing angle but also suggest that the Yokoya factor is constant, or varies weakly, with the crossing angle. It is worth noting that for a half crossing angle greater than 300 μrad, the uncertainty on ΔQ increases (Fig. 6). This effect is caused by a broadening of the peak corresponding to the π-mode in the beam oscillation spectrum, as illustrated in Fig. 7b. For such angles, the frequencies covered by the incoherent spectrum due to the non-linearity of the beam-beam force reaches the frequency of the π-mode, thus resulting in Landau damping of the coherent mode.

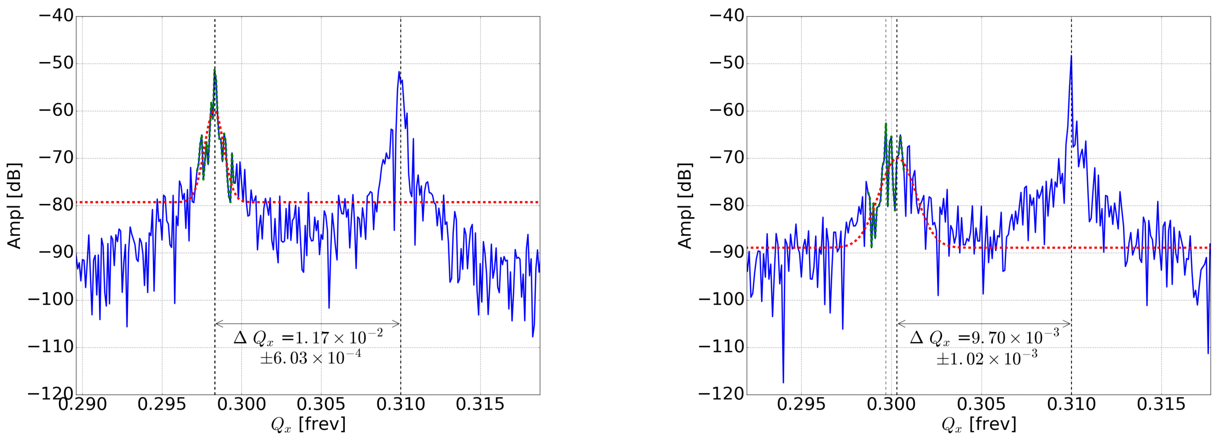

(a) For 100 μrad of half crossing angle. (b) For 400 μrad of half crossing angle.

Figure 7: Beam oscillation spectrum extracted from Fig. 5. The Gaussian fit performed to evaluate the error on the frequency of π-mode, is shown with a dashed red line. The peak is marked with a grey vertical line. The results of the fits were reported in Fig. 6.

2.3 Limit of the frozen model: π-mode instability

The frozen model exhibits artificial coherent instabilities when pushed beyond its validity, i.e. when $\chi_{\text{frozen}} \approx 1$ or higher. Two examples of such artificial instabilities are described below, together with the corresponding simulations using the full model, which does not feature this instability.

2.3.1 Decoherence studies

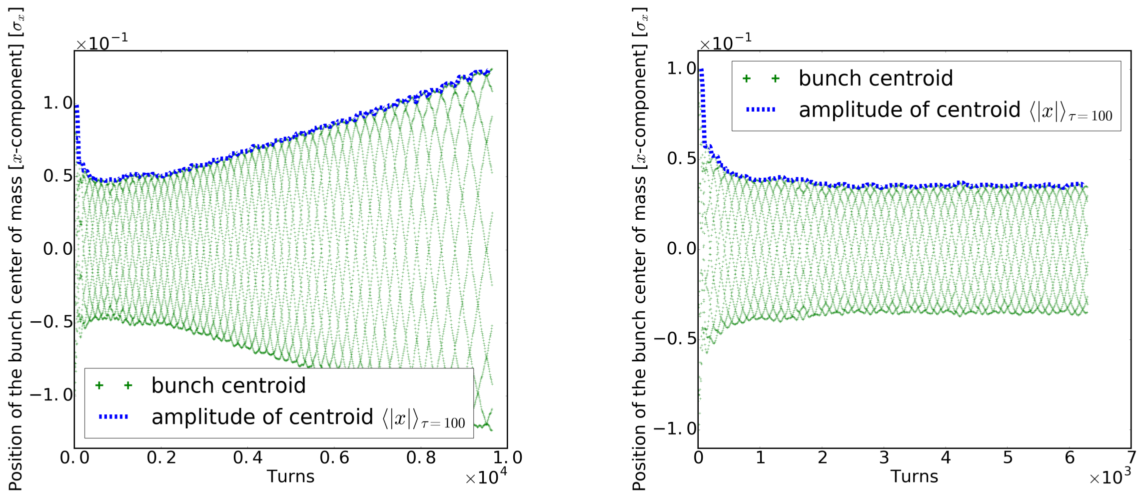

(a) Frozen model. (b) Full model.

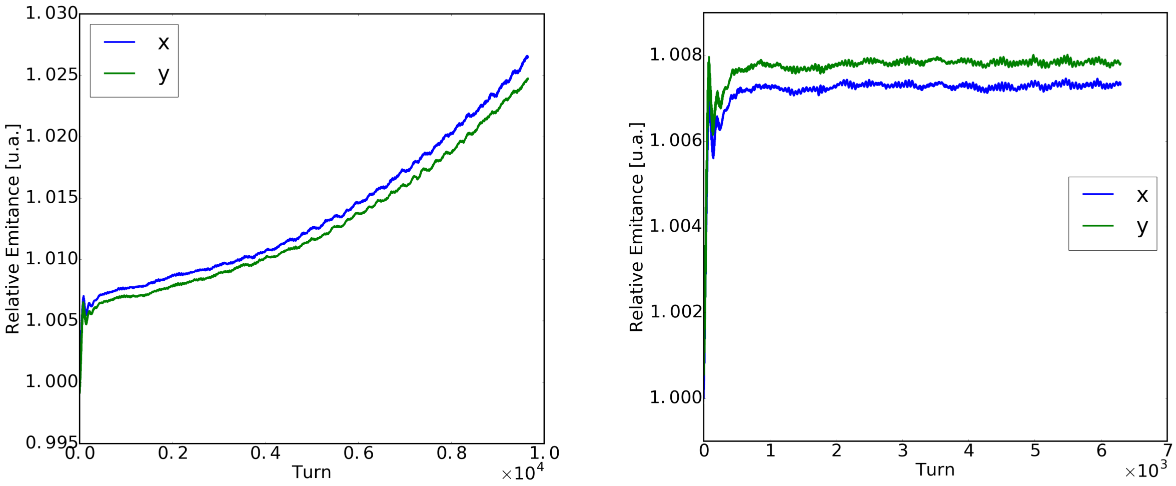

(c) Frozen model. (d) Full model.

Figure 8: Observation of the decoherence of the π-mode for a large beam-beam parameter $\xi = 3.2\ Q_S$ and a strong hourglass $\sigma_s/\beta^* = 0.45$, resulting in $\chi_{\text{frozen}} = 0.04$. The simulation is performed with the 6D soft-Gaussian frozen model and a linear lattice.

The decoherence of a kick applied to the colliding beams will be discussed in the next section, here we discuss a numerical instability that was encountered with the frozen model. The simulation setup for these studies consist in initialising the two beams with an offset with respect to their reference orbit. In order to initialise the beams in a σ-mode configuration, the two beams are offset in the same direction, as opposed to the π-mode configuration in which the two bunches are initialised with opposite offsets. The beam parameter evolution during a simulation of the decoherence of the π-mode with a large beam-beam parameter and a strong hourglass effect is shown in Fig 8. Both the oscillation amplitude and the beam emittance are growing in time, indicating the presence of a numerical instability. The parameters chosen correspond to $\chi_{\text{frozen}} = 0.04$. This numerical artefact of the frozen model is not present when using the full implementation of the coherent 6D kick for the same simulation setup.

2.3.2 Impedance studies

A similar numerical instability is observed in the presence of wake fields but without initial offset. We consider here a similar configuration with a single IP and two identical optics for the two beams, a strong hourglass effect and without crossing angle. Figure 9 shows the comparison of the complex frequencies obtained for this configuration with varying beam-beam parameter, at a fixed effect of the wake fields, with three models: the frozen model, the full model and the linearised modal approaches. For both 6D soft-Gaussian model we observe a good correspondence with the linearised modal approach only for the low beam-beam parameter ($\xi \lessapprox Q_s$). For $Q_s \lessapprox \xi \lessapprox 8Q_s$, we observe the damping of the mode coupling instabilities in both macro-particle approaches as opposed to the linearised modal approach. This effect can be attributed to Landau damping by the synchrotron side-bands, as will be discussed in the next sections. For a beam-beam parameter larger than $\approx 8Q_s$, corresponding to $\chi_{\text{frozen}} \approx 0.08$, an instability of the π-mode is observed only in the frozen model. As in the decoherence studies, this instability is a numerical artefact.

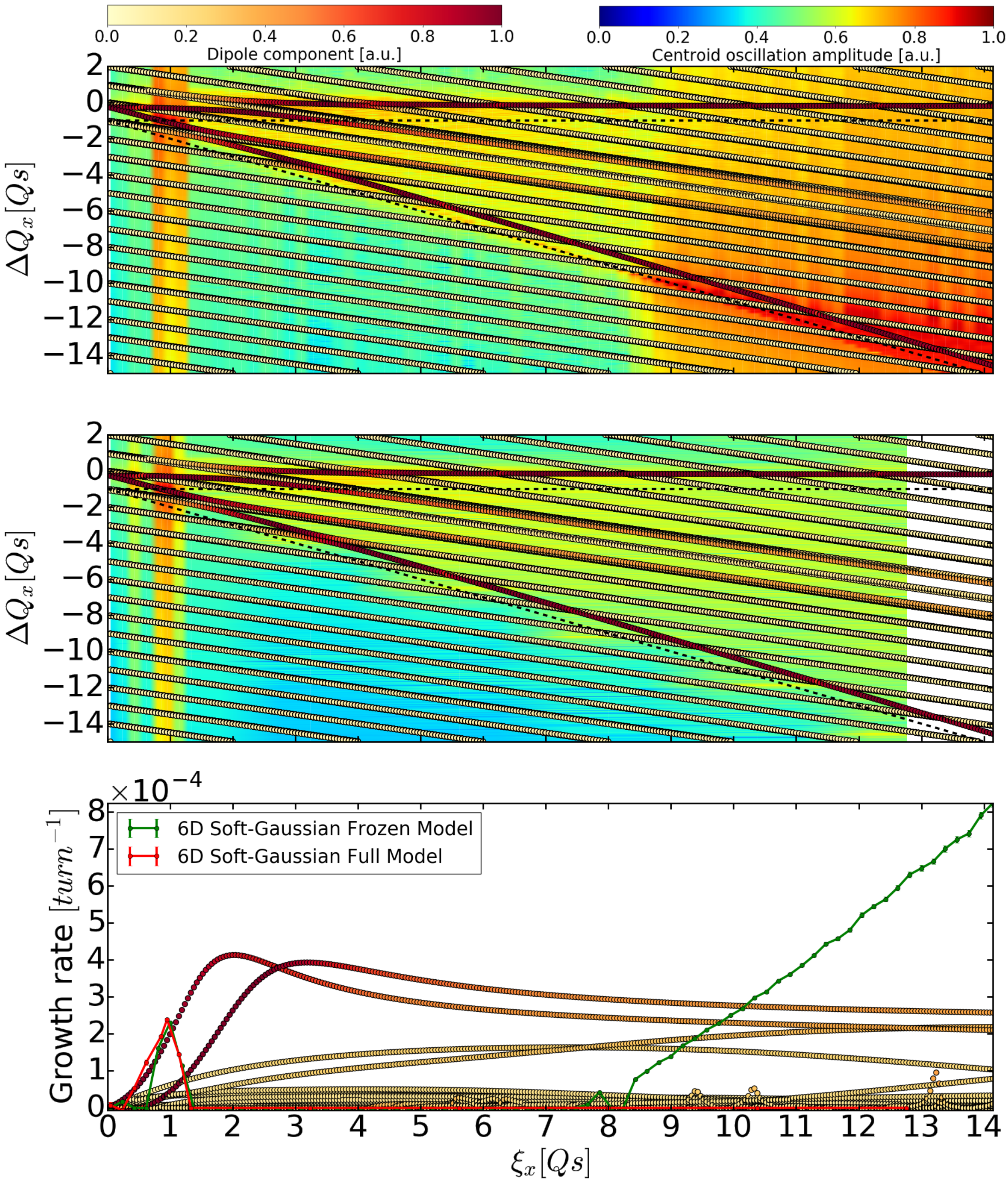

Figure 9: Comparison of the complex tune shifts obtained with the modal approach using *BimBim* (dots colorcoded in red to yellow corresponding to large to small dipolar moments) and the spectrum (colour coded on the two upper plots) and growth rate (lower plot) obtained with the macro-particle approach with *COMBI*, using the frozen and full 6D soft-Gaussian coherent beam-beam kick. The simulation were performed with the HL-LHC parameters listed in Tab. 1 but without crossing angle and a single 6D beam-beam interaction. The number of macro-particles is 10^6 and the number of longitudinal slices is 50. For the modal approach, the longitudinal phase space is modelled with 50 slices and 5 rings. The effect of the wake fields are kept constant while scanning the beam-beam parameter. The upper and lower limit of the single particle frequencies in the lower synchrotron side-band are represented in dotted lines to guide the eye.

It is worth noting here that the computing time using the frozen model for this configuration, featuring 10^6 macro-particles and 50 longitudinal slices, is about 6 times faster than the full model, bringing the execution time for a single simulation from about a week for the full model to about a day with the frozen model. Nevertheless, these models seem limited to configurations with χ_{frozen} in the order of a few percent.

3 Hourglass effect

Based on the development in [5], one does not expect any decoherence, and consequently any Landau damping of both the σ and π-modes, in a configuration without synchrobetatron coupling. Indeed, the latter, together with the overlap of the synchrotron side-bands of the spectrum of the single particles oscillating at different amplitudes, so-called incoherent spectrum, with the frequency of the coherent modes, also called discrete modes, were shown to be required conditions for both decoherence and Landau damping of these modes. In particular, it is also shown that in the presence of both hourglass effect and chromaticity, the coupling between the longitudinal plane and the transverse plane is cancelled with the condition :

$$\frac{Q'\sigma_s}{\alpha_p R} = \frac{\sigma_s}{\beta_x^*}, \tag{3.1}$$

with the lattice chromaticity Q', the momentum compaction factor α_p and the machine average radius R. It is therefore expected to recover the loss of Landau damping and lack of decoherence if this condition is met. In the following, these results are verified and further extended with the new implementation of the 6D coherent kick in terms of both decoherence and Landau damping.

3.1 Decoherence

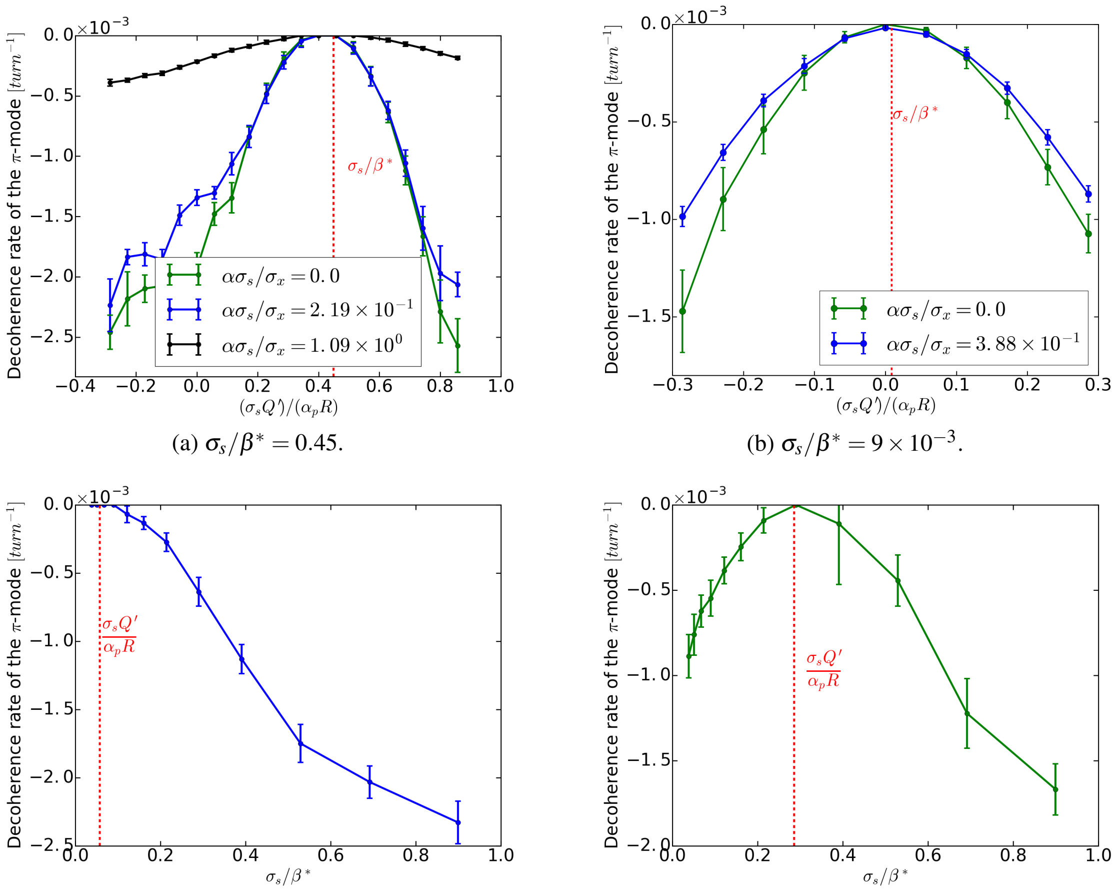

(a) $\sigma_s/\beta^* = 0.45$.

(b) $\sigma_s/\beta^* = 9\times10^{-3}$.

(c) $\sigma_s Q'/\alpha_p R = 0.057$.

(d) $\sigma_s Q'/\alpha_p R = 0.29$.

Figure 10: Simulated decoherence rate of the π-mode for different configurations of chromaticity, hourglass and crossing angle with a fixed beam-beam parameter of $\xi = 2.86\ Q_s$. The initial separation corresponds to $0.1\ \sigma_x$. The simulations were performed with a single 6D frozen soft-Gaussian coherent kick and a linear lattice over 10000 turns, using 10^6 macro-particles and 50 longitudinal slices.

Figures 10 shows the result of simulations of the decoherence time of the π-mode, obtained by initialising the position of both beams with an offset with respect to the closed orbit, in opposite directions. The decoherence time is obtained with an exponential fit of the decaying oscillation amplitude. A configuration compatible with the assumption behind Eq. 3.1 was chosen, with a single interaction point and an identical lattice for each beam. In the various configurations of chromaticity, hourglass effect and crossing angle, the absence of decoherence is recovered when the condition of Eq. 3.1, marked in red on the plots, is met. In all other cases, decoherence is observed as expected.
We observe that the decoherence decreases with the crossing angle α, as it could be anticipated since the tune spread induced by beam-beam interaction reduces.

The results of a similar set of simulations is shown in Fig. 11, in which the wake fields were introduced, based on the HL-LHC and LHC models. The difference in wake models does not play a role in this study, however we note that in the LHC-like configuration, with a low hourglass effect, the absence of decoherence is maintained in the presence of wake fields. On the other hand, in the HL-LHC-like configuration, featuring a large hour-glass effect, the absence of decoherence is not recovered. This can be explained as the condition of Eq. 3.1 results from a subtle cancellation of the synchrobetatron coupling term, which is broken by the wake fields. Indeed, the wake fields are a strong coherent source of synchrobetatron coupling which is not taken into account in the underlying model. This effect is critical in the understanding of mode coupling instabilities of colliding beams, as the effect of the wake fields can not be neglected. As a result, it is no longer expected to find configurations were the Landau damping is lost, as long as the condition of overlap between the incoherent spectrum and the coherent mode is met. Simulations are nevertheless still required to assess whether the Landau damping in such configurations is sufficiently strong to mitigate the mode coupling instability of colliding beams for a given wake field model.

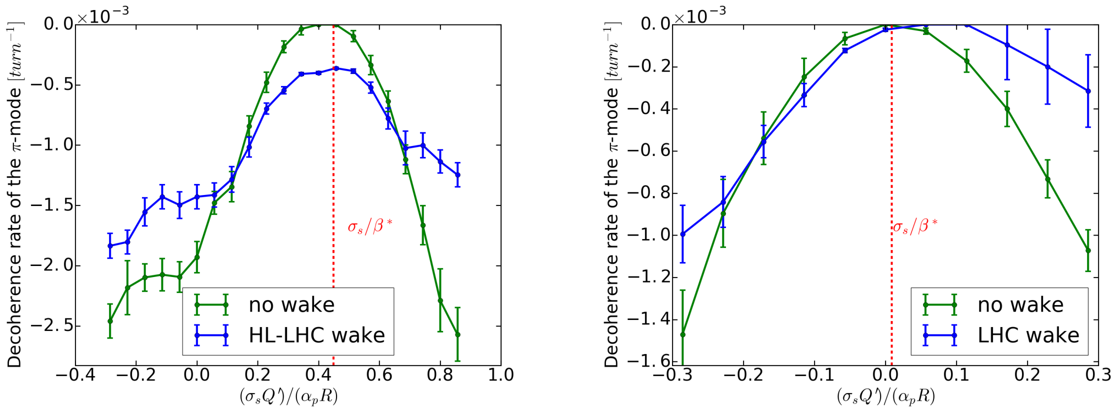

(a) $\sigma_s/\beta^* = 0.45$.

(b) $\sigma_s/\beta^* = 9 \times 10^{-3}$.

Figure 11: Simulated decoherence rate of the π-mode as a function of the chromaticity for a fixed beam-beam parameter $\xi = 2.86\ Q_s$ and different strengths of hourglass effect. The initial separation corresponds to $0.1\ \sigma_x$. The simulations were performed with a single 6D frozen soft-Gaussian coherent kick and a linear lattice over 10000 turns, using 10^6 macro-particles and 50 longitudinal slices.

3.2 Landau Damping of the mode coupling instability

The mode coupling instability of colliding beams, in absence of hour glass effect and chromaticity, was shown to occur only when the condition of overlap of the mode frequencies is met, similarly to the Transverse Mode Coupling Instability (TMCI). However, the mode coupling instability exists at any beam-beam tune shift in the presence of either hour glass effect or chromaticity. This effect is clearly observed in Fig. 12a where, for a strong hourglass effect, unstable modes are already visible for a low tune shift. In other words, the destabilising effect of the beam-beam interaction exists even when the frequency of the coherent modes are well separated. This can be understood as the head and the tail of the bunch are no longer only coupled through the wake fields, but also through the beam-beam force due to the variation of the beam size along the interaction. The TMCI-like behaviour is recovered when the hourglass effect is reduced, as shown by Fig. 12b.

The growth rate of the instability obtained with the macro-particle simulations are compatible with the most unstable mode obtained with the linearised modal approach for low beam-beam parameter. Once the beam-beam interaction is sufficiently strong, such that the π-mode enters the first lower synchrotron side-band of the incoherent spectrum, the instability is naturally damped. This damping for large beam-beam parameters can be interpreted as an effect of Landau Damping on the mode coupling instability of the colliding beam. Indeed, both the conditions of overlap of the coherent mode with the incoherent spectrum and the presence of synchobetatron coupling [5] are met. This interpretation is also compatible with the corresponding decoherence simulations (Fig. 12b). Indeed, the decoherence is inexistent for small tune shift, but increases significantly for both the σ and π-modes when their frequencies reach the first upper and lower sideband of the incoherent spectrum respectively.

The beam-beam force is such that the particles with a low oscillation amplitude experience a large tune shift downwards when considering particles of the same charge sign in each beam, whereas the particles with a large oscillation amplitude see a vanishing force and consequently a vanishing tune shift. As a result, the σ-mode lays naturally at the upper end of the incoherent spectrum. Since we consider here a wake field model dominated by resisitve wall contributions, in particular due to collimators, the tune of the σ-mode is naturally shifted down towards the incoherent spectrum. It is therefore expected that as the wake fields strength increases, the decoherence and Landau damping of this mode increases as well. This effect is shown with a decoherence simulation of the σ-mode in the presence of wake fields in Fig. 12a. This effect does not apply to the π-mode, whose frequency lays below the incoherent spectrum.

For weak hourglass effect, the absence of damping for the first mode coupling (π-mode and azimuthal head-tail mode -1) is expected in absence of synchrobetatron coupling and is also compatible with the absence of decoherence in the simulation. The damping of the second coupling (σ-mode and azimuthal head-tail mode +1) seem however in disagreement with both. Yet, as shown in the previous section, the synchrobetatron coupling induced by the wake itself can restore Landau damping. Here, we can interpret the difference of behaviour between the two mode couplings by noticing that the frequency of the first occurs at the upper part of the first lower sideband of the incoherent spectrum, whereas the second coupling occurs in the middle of the upper sideband. Since the centre of the spectrum is significantly more populated than the edge, the Landau damping is expected to be more efficient for the second coupling. This explanation was already discussed in [2].

Finally, comparing the real tune shift obtained with the macro-particle simulations with respect to the linearised modal approach, one observes a slight difference, due to the Yokoya factor, equal to 1.1 for the macro-particles simulations using the soft-Gaussian model and 1.0 in the linearised model. As a result, the mode coupling instability occurs at a slightly different frequency.

4 Application to the HL-LHC configuration

Thanks to the establishment of collisions with a large β^*, allowing for luminosity levelling and the par-

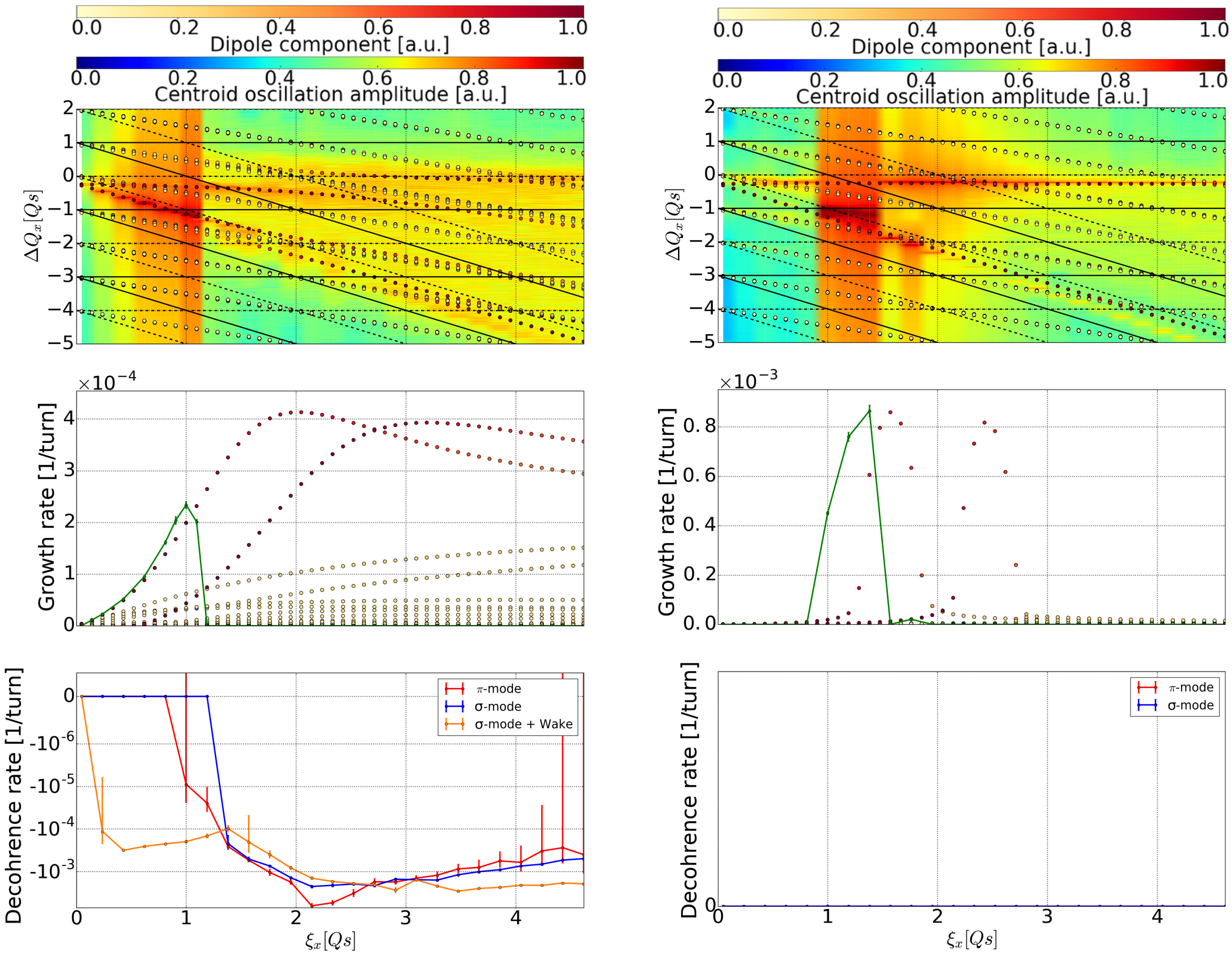

(a) HL-LHC case.

(b) Low hourglass.

Figure 12: Simulations of the mode coupling instability of colliding beams with a varying beam-beam tune shift using the macro-particle model with a single coherent 6D frozen beam-beam interaction and an identical lattice for both beams (upper and middle plots) as well as decoherence rate simulations in the same configuration (lower plots). When applicable, the effect of the wake fields is kept constant over the scan. On the upper plot, the spectrum of the beam oscillations (colour coded) is compared to the real tune shift obtained with the linearised modal approach (Dots shaded linearly from red to yellow with the corresponding dipolar moment of the mode from large to small). To guide the eye, the upper and lower end of the incoherent spectrum as well as its sidebands are marked with black lines, alternating solid and dashed for odd and even sidebands. The middle plots show a comparison of the fitted growth rate of the most unstable mode in macro-particle simulations (green lines) with the one derived from the complex tune shift of the linearised modal approach (dots shaded according to the dipolar moment). The left plot corresponds to the HL-LHC configuration (Tab. 1) without crossing angle, featuring a strong hourglass effect, whereas the right plot corresponds to the benchmark configuration (Tab. 1) without crossing angle featuring a low hourglass parameter and is therefore comparable to the configuration studied in [2]. The macro-particle simulations were performed with 10^6 macro-particles, 50 longitudinal slices over $7.5 \cdot 10^4$ turns. Both the evolution of the dipolar moment and of the transverse emittances are fitted with exponentials, the fastest of the two is reported here. The linearised model is based on 50 slices and 5 rings.

tial compensation of the crossing angle with crab cavities [16], the transverse feedback is expected to be efficient against the mode coupling of colliding beams [2] when the intensity is the highest, i.e. at the start of collision. In the following, we first study a pessimistic configuration for which the beam intensity would have been preserved until the establishment of the lowest β^*. Secondly, we study the impact of the absence of crab cavity for the same configuration. Following the discussions above, we expect that Landau damping by the synchrotron side-bands will occur in all these configurations. With these simulation we quantify whether its strength is sufficient to maintain the beam stability, even in configurations for which the transverse feedback acting on the dipole component of the oscillation is not sufficient to fully suppress the mode coupling instability of colliding beams.

Figure 13a shows the complex tune shifts of the coherent modes obtained with the modal approach for the HL-LHC configuration when the crossing angle is partially compensated by crab cavities, varying the strength of the beam-beam interaction while maintaining the interactions with wake fields at a constant value, corresponding to the nominal bunch intensity. As expected from the analysis in the previous sections, there exists mode coupling instabilities at all beam-beam parameters. The different radial modes associated to the same azimuthal mode (i.e. with frequencies degenerated at a given synchrotron side band) are affected differently by the beam-beam interaction due to their different longitudinal mode pattern. As a consequence, the degeneracy in the mode frequency is lifted, visible with a splitting of the lines in the real part of the tune shift for increasing beam-beam tune shift (upper

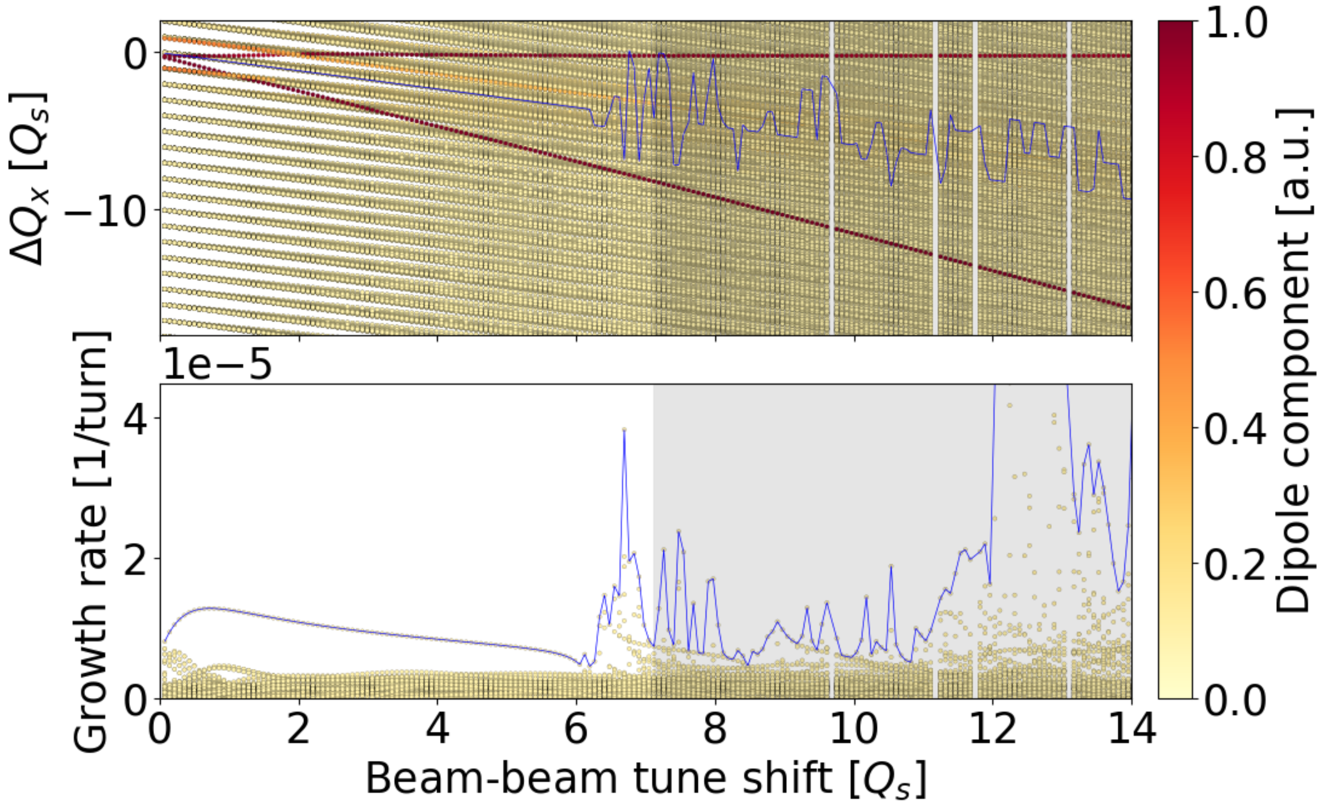

(a) BimBim

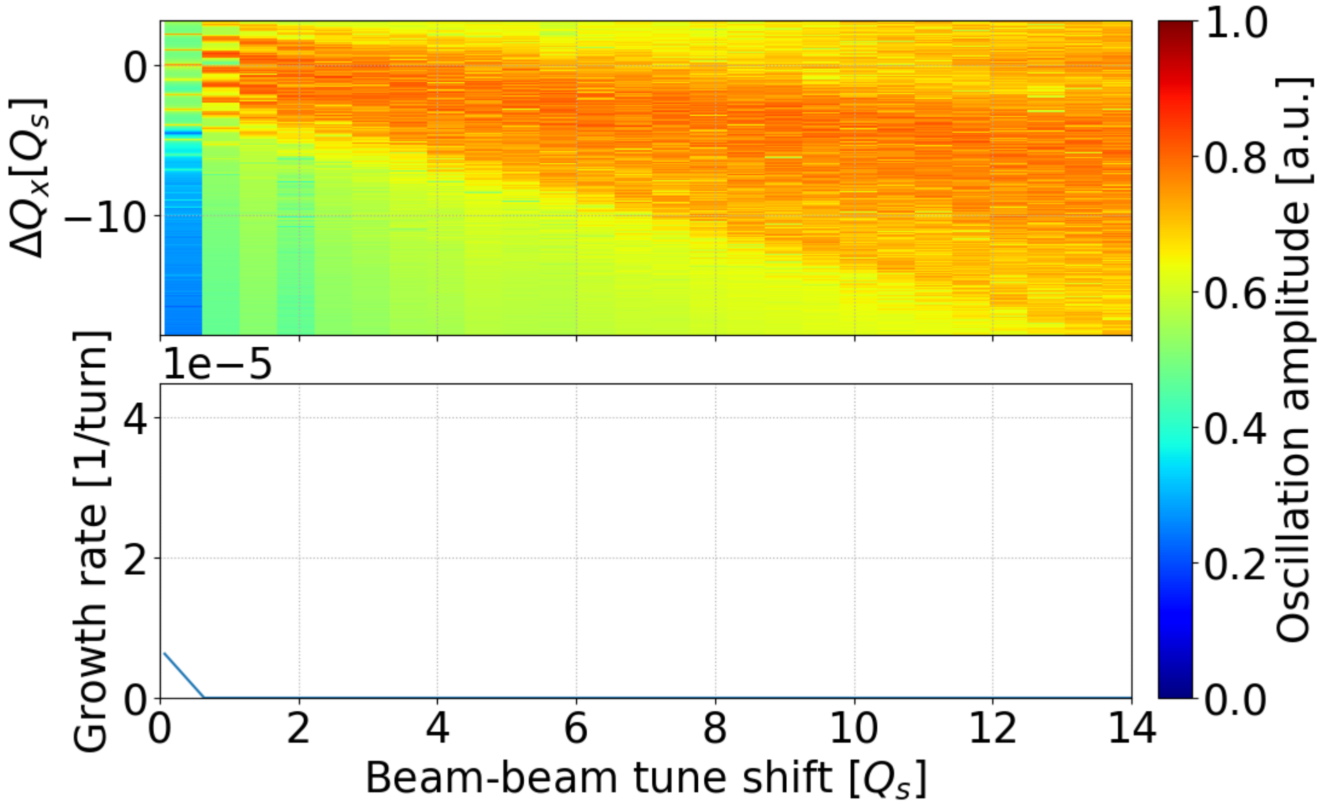

(b) COMBI

Figure 13: Comparison of the results of the modal analysis with *BimBim* (upper plot) and the spectrum and growth rates obtained with the macro-particle approach with *COMBI* (lower plots). The simulations were performed with the parameters of the HL-LHC (Tab. 1), including the wake fields effect, the lattice with a chromaticity of 15 units, the beam-beam interactions (6D soft-Gaussian kick for macro-particle approach) at the two main IPs with crossing angles in alternated planes and a transverse feedback with gain 0.01 (corresponding to a damping time of 200 turns). The effect of the wake fields is kept constant over the scan in beam-beam parameter. The simulations were performed with 10^6 macroparticles over $2 \cdot 10^5$ turns. For the modal approach the longitudinal phase space was represented by 60 slices and 15 rings. The shaded areas represents beam-beam parameters that cannot be achieved with the expected beam parameters. In the upper plots, the blue lines highlight the real and imaginary part of the most unstable mode.

plot in Fig. 13a). For beam-beam tune shifts above $\approx 2Q_s$, the radial modes frequencies start to overlap with other side bands leading to a forest of mode couplings between high order head-tail modes through the 6D beam-beam interactions.
By comparing with the result of the corresponding macro-particle tracking simulations shown in Fig. 13b, we observe that most of these instabilities are suppressed through the Landau damping mechanism discussed in the previous sections. The only instability remaining appears at low beam-beam tune shift, i.e. well below the synchrotron tune corresponding to the configuration when Landau damping by synchrotron side-band can not occur. This instability is not expected to limit the HL-LHC as such low beam-beam tune shifts are not achieved in normal conditions. Indeed, to perform optimally the intensity decay is limited [16], resulting in minimum beam-beam tune shifts well above the synchrotron tune.

The results of simulations in a similar configuration but without crossing angle compensation by the crab cavities are shown in Fig. 14. We note that the beam-beam tune shift due to the two IPs takes into account the reduction to the crossing angle using Eq. 2.32 and is therefore significantly reduced with respect to the configuration with crab cavities. Nevertheless, similar conclusions may be drawn in this configuration as the presence of strong synchrobetatron coupling allows for Landau damping of all the mode coupling instabilities of higher order head-tail modes.

We note that the linearised model (Figs. 13a and 14a), does not include the Yokoya factor, which explains the small difference with respect to the extend of the beam spectrum shown in Figs. 13b and 14b respectively. The growth rate obtained for small beam-beam tune shift, i.e. in absence of Landau damping, are in good agreement between the models, for both the configurations considered.

5 Conclusion

In order to study efficiently the mode coupling instability of colliding beams in realistic configurations of the HL-LHC, featuring strong synchrobetatron coupling, new numerical algorithms were implemented in the multiparticle tracking code COMBI. First a full implementation of the 6D coherent beam-beam interaction, based on Hirata's incoherent model, describing the evolution of the distribution of both beams as they travel through each other, in a boosted frame where electromagnetic forces between the beams can be expressed conveniently, was implemented, similarly to the existing code BeamBeam3D. The need for update of the particles momentum through each beam-beam interaction is however shown to be superfluous in configurations where the beam-beam interaction is sufficiently weak, thus allowing for computationally efficient algorithm, the so-called *frozen 6D model*. These models were successfully benchmarked against predictions from analytical models.
It is shown that the mode coupling instability of colliding beams is well suppressed by Landau damping when the frequencies of the coherent modes overlaps with the synchrotron side-bands of the incoherent spectrum, as predicted qualitatively by theoretical models. Moreover, the link between decoherence and Landau damping is emphasised also in simulation. In particular, it is shown that the coherent tune shift induced by the impedance can, in certain conditions, bring the σ-mode back in the incoherent spectrum thus restoring Landau damping and decoherence. This stabilisation mechanism for high intensities is understood but was not anticipated.
The application of this method to the HL-LHC configurations suggest that Landau damping is sufficient to ensure the stability in all realistic configurations with beams colliding head-on.

Acknowledgement

This research is supported by the HL-LHC project.
The authors would like to thank the Laboratoire de Physique des Accélérateur de particules at the Ecole Polytechnique Fédérale de Lausanne for providing important computing resources, as well as the CERN IT group for deploying new high performance computer cluster. Both resources were necessary for this study.
J. Barranco and T. Van Daalen contributed to this study by providing initial steps in the development of the implementation of the 6D coherent beam-beam lens in *COMBI*. This study greatly profited as well from fruitful discussions with Y. Alexahin, in particular from his proposal to compare decoherence time to predictions of the Vlasov perturbation theory, and with S. Antipov. The authors would like to thank them warmly.
The authors would also like to thank E. Métral and G. Arduini for their comments on this manuscript.

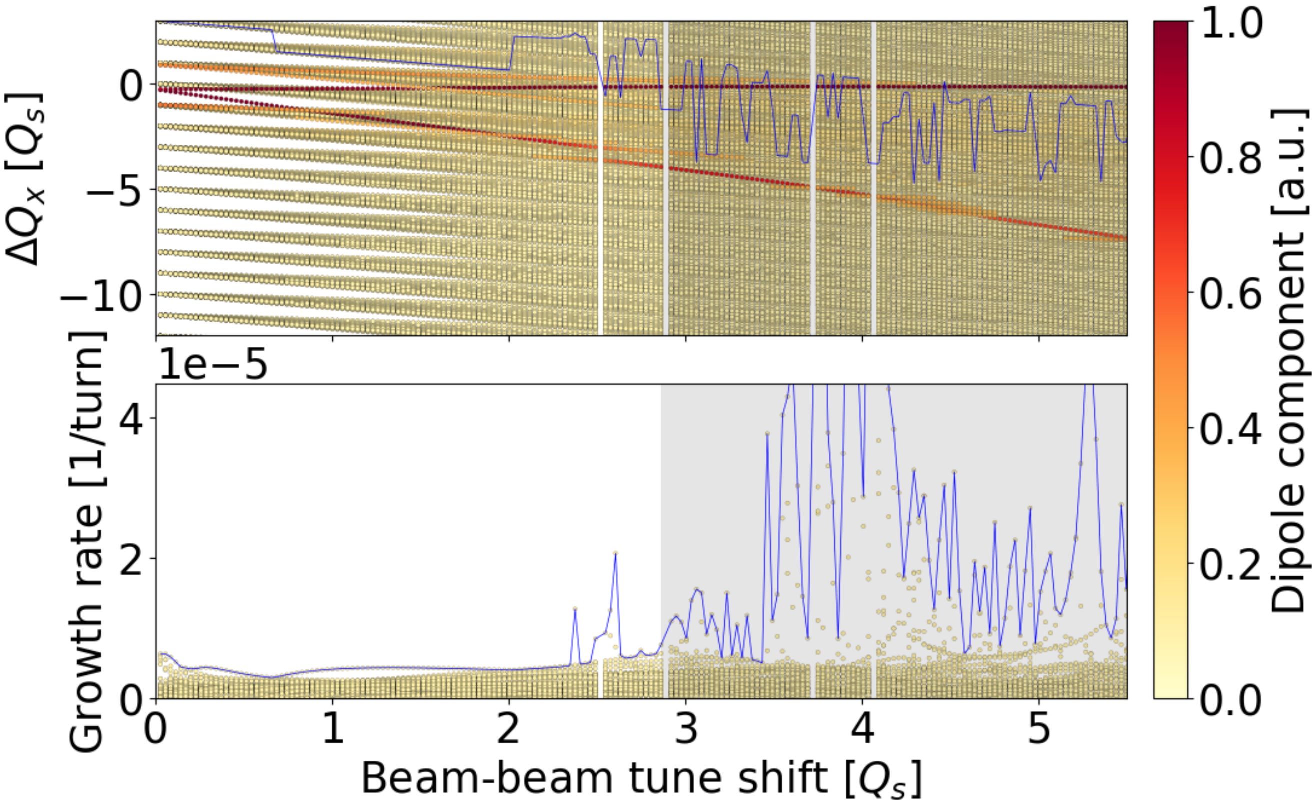

(a) BimBim

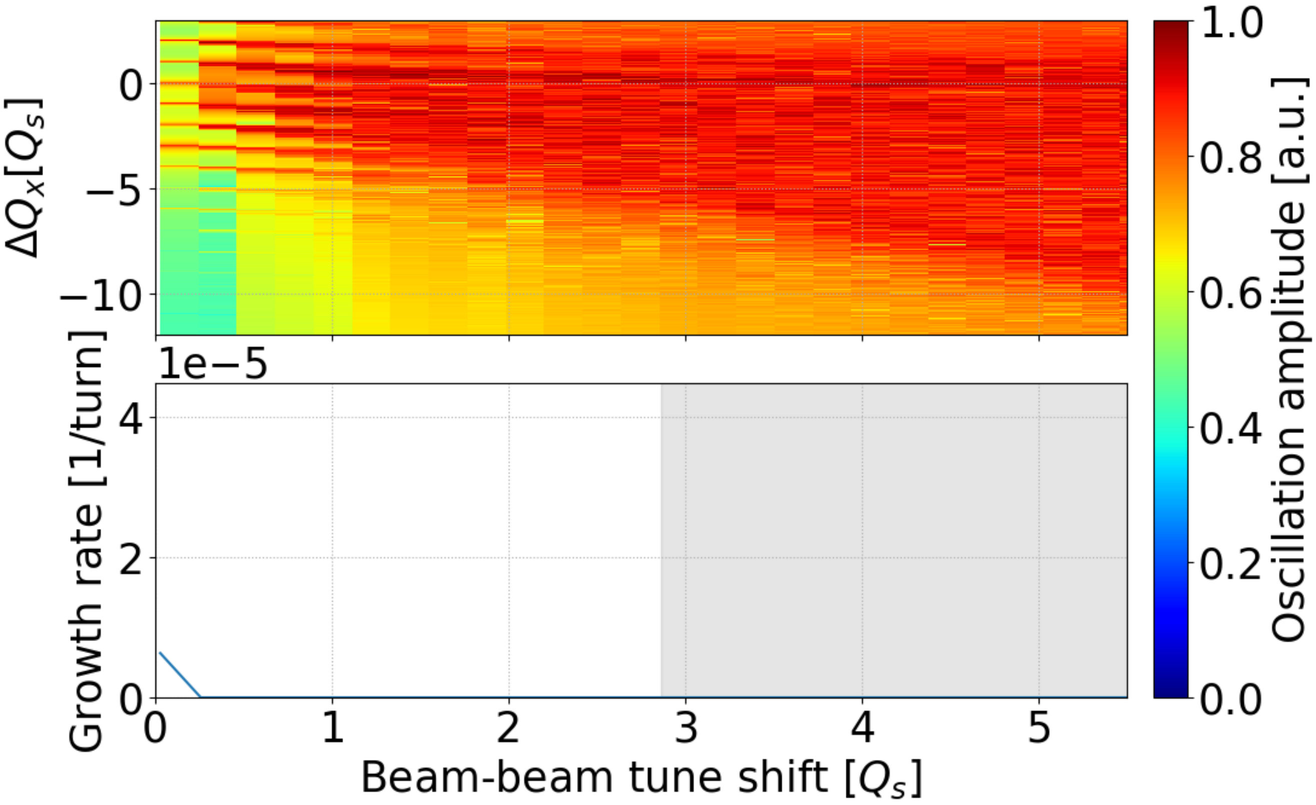

(b) COMBI

Figure 14: Comparison of the results of the modal analysis with *BimBim* (upper plot) and the spectrum and growth rates obtained with the macro-particle approach with *COMBI* (lower plots). The simulations were performed with the parameters of the HL-LHC (Tab. 1) without crab cavities, i.e. a full crossing angle of 500μrad. The simulation include the wake fields effect, the lattice with a chromaticity of 15 units, the beam-beam interactions (6D soft-Gaussian kick for macro-particle approach) at the two main IPs with crossing angles in alternated planes and a transverse feedback with gain 0.01 (corresponding to a damping time of 200 turns). The effect of the wake fields is kept constant over the scan in beam-beam parameter. The simulations were performed with 10^6 macroparticles over $2 \cdot 10^5$ turns. For the modal approach the longitudinal phase space was represented by 60 slices and 15 rings. The shaded areas represents beam-beam parameters that cannot be achieved with the expected beam parameters. In the upper plots, the blue lines highlight the real and imaginary part of the most unstable mode.

Bibliography

[1] K. Hirata, H. W. Moshammer, and F. Ruggiero, "A symplectic beam-beam interaction with energy change," Part. Accel. **40**, 205 (1992).

[2] S. White, X. Buffat, N. Mounet, and T. Pieloni, "Transverse mode coupling instability of colliding beams," Phys. Rev. ST Accel. Beams **17**, 041002 (2014).

[3] X. Buffat, J. Barranco, T. Pieloni, C. Tambasco, "Effect of the crossing angle on coherent stability, Presentation at the HL-LHC WP2 meeting, 20th sept. 2016," `https://indico.cern.ch/event/563293/contributions/2316566/attachments/1352296/2041874/2016-09-20-expanded.pdf`, accessed: 2017-06-02.

[4] X. Buffat, *Transverse beams stability studies at the Large Hadron Collider*, Ph.D. thesis, EPFL (2015), CERN-THESIS-2014-246.

[5] Y. Alexahin, "A study of the coherent beam-beam effect in the framework of Vlasov perturbation theory," Nucl. Instrum. Methods Phys. Res. A **480**, 253 (2002).

[6] W. Herr and R. Paparella, *Landau damping of coherent beam-beam modes by overlap with synchrotron sidebands*, LHC Project Note 304 (CERN, Geneva, Switzerland, 2002).

[7] J. Qiang, M. A. Furman, R. D. Ryne, W. Fischer, and K. Ohmi, "Recent advances in strong-strong beam-beam simulation," Nucl. Instrum. Meth. **A558**, 351 (2006).

[8] X. Buffat, "Coherent beam-beam effects," CERN Yellow Reports: School Proceedings **3**, 391 (2017).

[9] T. Pieloni, *A study of beam-beam effects in hadron colliders with a large number of bunches*, Ph.D. thesis, EPFL (2008), CERN-THESIS-2010-056.

[10] W. Herr, M. P. Zorzano, and F. Jones, "Hybrid fast multipole method applied to beam-beam collisions in the strong-strong regime," Phys. Rev. ST Accel. Beams **4**, 054402 (2001).

[11] K. Hirata, "A computer code for beam-beam interaction with a crossing angle, version 3.4," BBC user's guide (1997).

[12] K. Yokoya, E. Kikutani, Y. Funakoshi, J. Urakawa, and H. Koiso, "Tune shift of coherent beam-beam oscillations," Part. Accel. **27**, 181 (1989).

[13] L. H. A. Leunissen, F. Schmidt, and G. Ripken, "Six-dimensional beam-beam kick including coupled motion," Phys. Rev. ST Accel. Beams **3**, 124002 (2000).

[14] G. Iadarola, R. De Maria, and Y. Papaphilippou, *6D beam-beam interaction step-by-step*, CERN-ACC-NOTE-2018-0023 (CERN, Geneva, Switzerland, 2017).

[15] R. M. Corless, G. H. Gonnet, D. E. Hare, D. J. Jeffrey, and D. E. Knuth, "On the LambertW function," Advances in Computational mathematics **5**, 329 (1996).

[16] E. Métral, S. Antipov, F. Antoniou, R. Appleby, G. Arduini, J. Barranco, P. Baudrenghien, N. Biancacci, C. Bracco, R. Bruce, X. Buffat, R. Calaga, L. Carver, M. Crouch, R. D. Maria, S. Fartoukh, D. Gamba, M. Giovannozzi, P. Gonçalves Jorge, W. Hofle, G. Iadarola, N. Karastathis, A. Lasheen, K. Li, T. Mastoridis, L. Medina, A. Mereghett, D. Mirarchi, B. Muratori, S. Papadopoulou, Y. Papaphilippou, D. Pellegrini, T. Pieloni, S. Redaelli, G. Rumolo, B. Salvant, E. Shaposhnikova, M. Solfaroli, C. Tambasco, R. Tomàs, and D. Valuch, *Update of the HL-LHC Operational Scenarios for Proton Operation*, CERN-ATS-Note-2018 (CERN, Geneva, Switzerland, 2018).

[17] N. Biancacci, B. Salvant, E. Métral, K. Li, "The HL-LHC impedance model and aspects of beam stability," in *Proceedings of IPAC 2016, Busan, Korea* (CERN).

[18] `https://impedance.web.cern.ch/impedance/`.